



Characterization and thermoelectric properties of polyol method-synthesized $(\text{Cu}_7\text{Te}_4)_{1-x}(\text{Ag}_2\text{Te})_x$ ($x = 0, 0.03$) nanocomposites

Chanderbhan Chotia¹, Gunadhor Singh Okram^{1,*} , and Bodhoday Mukherjee¹

¹UGC-DAE Consortium for Scientific Research, University Campus, Khandwa Road, Indore-452001, Madhya Pradesh, India

Received: 22 July 2020

Accepted: 4 October 2020

Published online:

13 October 2020

© Springer Science+Business Media, LLC, part of Springer Nature 2020

ABSTRACT

$(\text{Cu}_7\text{Te}_4)_{1-x}(\text{Ag}_2\text{Te})_x$ ($x = 0, 0.03$) nanocomposites (NCs) of crystallite size in the range of 23–31 nm have been synthesized successfully using only diethylene glycol. Detailed characterizations show the single-phase and disk-shaped nanoparticles (NPs) of hexagonal Cu_7Te_4 with average thickness of 42 nm and width of 75 nm. Hydrodynamic diameter is found to be in the range of 308–351 nm and the zeta potential values indicate that the NCs are dispersible and stable in deionized water. Small positive Seebeck coefficient α with relatively high electrical conductivity σ indicates their highly degenerate p-type semiconducting nature with a signature of the energy filtering in electron transport. The barrier heights of 1.4 and 4.1 meV for $x = 0$ and 0.03, respectively, confirm their highly degenerate semiconducting nature. The thermoelectric power factor of $9.7 \mu\text{W}/\text{mK}^2$ for 0.03 is nearly 45% enhancement compared to that of Cu_7Te_4 and 242 times that of $\text{Bi}_2-x\text{Cu}_x\text{S}_3$ NPs showing great potential of this approach.

1 Introduction

Nowadays, intense research is focused on generating useful energy at the cost of minimal environmental loss through less effort. In this direction, thermoelectric (TE) materials attract particular attention due to their ability to produce electricity silently using/consuming waste heat without generating harmful gases or by-products [1–4]. Thermoelectric (TE) devices without moving parts and without

pollution can be used for the strategic generation and cooling of solid bodies. Their efficiency is determined by the dimensionless figure of merit $ZT = (S^2\sigma/\kappa)T$, where S is the Seebeck coefficient, σ is the electrical conductivity, κ is the total thermal conductivity (due to the electronic κ_e and the lattice κ_L thermal conductivities), and T is the absolute temperature [5, 6]. However, these properties are interrelated in the usual materials, which always leads to a poor efficiency of a material and hence has limited its applications. The strategies for optimizing comprehensive

Address correspondence to E-mail: okram@csr.res.in

TE performance can be briefly described as power factor ($PF = S^2\sigma$) improvement or/and κ_L suppression. The synergetic achievement of both goals naturally leads to a maximum optimization of the ZT values. Nevertheless, due to the interdependency of the material properties, it remains the central challenge in this area. There are many reports to improve PF, e.g., the increase density of states (DOS) via band convergence [7] and resonant scattering [8]. Controlling the scattering process of charge carrier filtering is also one way to increase the PF [9–13]. Takafumi et al. proposed a new method for PF improvement by introducing coherent homoepitaxial interfaces with controlled dopant concentration [14].

$Cu_{2-\delta}Te$ ($0 \leq \delta \leq 1$) have been proposed as functional materials in thermoelectric, photothermal therapy, photovoltaics and batteries [15–18]. Hexagonal Cu_7Te_4 is also a stable phase of $Cu_{2-\delta}Te$ and shows a metallic conductivity with a relatively low Seebeck coefficient [19, 20]. The approach to producing nanocomposites (NCs) from metallic nanoparticles (NPs) in a matrix was also of interest, since a theoretical calculation predicted an improvement in ZT if metal nano-inclusions were incorporated into a semiconducting matrix [12]. This is attributed to a band bending at the metal–semiconductor interface, which creates a potential energy barrier that effectively blocks low-energy charge carriers while transmitting high-energy carriers [4]. As a result, the Seebeck coefficient is increased for a given carrier concentration because the charge of electrons is carried with a higher average energy per carrier [4, 19].

It has been reported that many synthetic approaches contain copper telluride NPs [20–26]. Tarachand et al. reported an improved thermoelectric performance of Ag-doped CuS NPs made by the polyol method in 2 h [27] and Ballikaya et al. Ag-doped Cu_2Te and Cu_2Se produced by melting, annealing and spark plasma sintering in over 10 days [16]. We synthesized $(Cu_7Te_4)_{1-x}(Ag_2Te)_x$ ($x = 0, 0.03$) NCs within 2 h using a simple polyol method that is slightly different from an earlier report [28]. With systematic characterizations, their thermoelectric properties were examined, which indicate the energy filtering of the electron transport. We therefore find a significantly enhanced Seebeck coefficient, PF and stable dispersibility that is of particular interest.

2 Experimental

2.1 Synthesis of $(Cu_7Te_4)_{1-x}(Ag_2Te)_x$ ($x = 0, 0.03$)

Cu_7Te_4 NPs have been synthesized successfully using a simple polyol method. In the previous report [28], we dissolved together $Cu(CH_3COO)_2 \cdot H_2O$ and $K_2TeO_3 \cdot H_2O$ as Cu and Te sources, respectively, in 2:1 ratio, in 50 ml diethylene glycol (DEG). In this report, we dissolved $Cu(CH_3COO)_2 \cdot H_2O$ and $K_2TeO_3 \cdot H_2O$ separately in 20 ml of DEG in each. After this, we mixed these solutions in a three-neck flask to prepare Cu_7Te_4 and heated at the rate of $25 \text{ }^\circ\text{C min}^{-1}$ to $200 \text{ }^\circ\text{C}$ in argon atmosphere; the color of the solution changes from sky blue to dark brown. For a complete reaction, the temperature was maintained for 2 h. It should be pointed out that optimization of reaction parameters like reaction time and temperature were checked. Reaction takes place above $190 \text{ }^\circ\text{C}$, and $200 \text{ }^\circ\text{C}$ was found to be reasonable or optimum. Then, the solution was cool down to room temperature in the natural way. Centrifugation for 12 min. at 12,000 rpm and decantation removed the precipitate from the suspension. The precipitate was then dispersed in ethanol and subjected to 5 min. of probe ultrasonication for uniform dispersion. The dispersed precipitate was then centrifuged for another 4 min. at the same rpm and the supernatant was decanted. These cleaning steps were repeated three times. Finally, the transparent layer of ethanol was discarded, and the precipitate was vacuum-dried at $60 \text{ }^\circ\text{C}$ for 5 h. The powder thus obtained was used for various characterizations and further processing. In this process, DEG was chosen as the solvent due to its excellent solubility of many metal salts, which makes it possible to bind and stabilize the metal. The solvent in the polyol process also acts as the absorber to release the excess heat generated in the reaction. The experimental results show that DEG is a good solvent in such synthesis processes due to its strong polarity. The same procedure was followed to obtain $(Cu_7Te_4)_{1-x}(Ag_2Te)_x$ ($x = 0.03$) using $Ag_2C_2H_3O_2 \cdot H_2O$ as the Ag source.

2.2 Characterization techniques used

The formation of a crystalline phase was confirmed from X-ray diffraction (XRD) patterns, which were collected using a Bruker D8 Advance X-ray

diffractometer with Cu K α radiation (1.54 Å) in an angular range (2θ) from 10° to 80° with a scanning angle size of 0.02°. To investigate the surface morphology of the nanoparticles, we performed field emission scanning electron microscopy (FESEM) measurements on pellets of these samples using a FEI Nova NanoSEM 450 instrument operating at 18 kV. Elemental analysis was performed by energy dispersive X-ray analysis (EDX) using a JEOL JSM 5600 scanning electron microscope. The hydrodynamic diameter (HD) and surface charge of the nanoparticles were measured in deionized water (as the suspension medium) at pH 7 and 25 °C using a zeta/particle size analyser (NanoPlus-3). The resulting NPs were consolidated under a uniaxial pressure of ~ 1 GPa to rectangular pellets of 8 mm \times 4 mm \times 2 mm in size at room temperature and then annealed in a tube furnace at 300 °C under a continuous Ar gas flow for 6 h. The Seebeck coefficient (S) was measured by a home-made load-based thermopower setup with a 8 mm diameter \times 1-mm-thick rectangular pellet clamped between the flat ends of two oxygen-free highly conducting cylindrical copper blocks [29] and resistivity was measured by four-point probe setup of the samples in the temperature range of 5–325 K (\pm 3% error) [30] in a specially developed commercial Dewar with differential direct current.

3 Results and discussion

3.1 X-ray diffraction and FESEM studies

Copper tellurides can exist in a variety of stoichiometric compositions [24, 25]. Their formation can be distinguished from the powder X-ray diffraction (XRD) patterns of the synthesized samples (Fig. 1a). Their peaks observed at approx. 12.2°, 24.7°, 35°, 39.6°, 41.6°, 43.4°, 45.1°, 50.6° and 65° in Cu₇Te₄ and (Cu₇Te₄)_{0.97}(Ag₂Te)_{0.03} could be attributed to hexagonal (P3m1) structure of Cu₇Te₄ (JCPDS card no. 652057) and matched with earlier report [28]. However, the extra peaks, not only the peaks due to the Cu₇Te₄ phase, are found that are well-matched with those of monoclinic Ag₂Te phase (JCPDS card no. 731755 and space group P2₁/c) (Fig. S1a) in the case of (Cu₇Te₄)_{0.97}(Ag₂Te)_{0.03}. These peaks are considerably broadened compared to the bulk material and are indicative of the nanoscale size of the NPs since in

the liquid synthetic system, complex chemical reaction process could contribute to the broadening of the XRD peaks [31]. The average crystallite size of the NPs was estimated to be 30.8 \pm 0.6 nm and 24.5 \pm 0.5 nm for (Cu₇Te₄)_{1-x}(Ag₂Te)_x ($x = 0, 0.03$), respectively using Scherrer formula based on the full width at half-maximum. It is 23.7 \pm 0.5 nm for Ag₂Te phase as determined from the average of the two peaks at 29.35° and 31.1°. Rietveld refinement fittings were performed for the XRD patterns (Fig. 1b, c); various parameters including χ^2 , Bragg R factor and RF factor are given in Table 1. While the peak intensities due to the Ag₂Te phase at 29.35° and 31.1° of the (-211) and (-212) planes are rather low (see star * in Fig. 1a, c) and hence expanded logarithmically (Fig. S1a), they can be confirmed and determined using the Rietveld refinement of (Cu₇Te₄)_{0.97}(Ag₂Te)_{0.03} (Fig. 1c). After successfully fitting Rietveld refinement, CIF file was generated for Cu₇Te₄ phase. Its crystal structure along the c -axis (or ab -plane) was generated using VESTA [32] software (Fig. 1d). It was found to be crystallized in a layered structure (Fig. S1). We have calculated some of the bond lengths (Table S1). The lowest bond lengths is found between Cu4-Cu6, while Cu2-Cu5 has the highest bond lengths in (Cu₇Te₄)_{1-x}(Ag₂Te)_x, $x = 0, 0.03$. The lattice constant specially 'a' or 'b' is slightly increased in (Cu₇Te₄)_{0.97}(Ag₂Te)_{0.03}, similarly the volume of the unit cells increases but the mass density is smaller than that of Cu₇Te₄ (Table 1). The density in our case is higher than that of Amiraslanov et al. [33].

The microstructure of the sample was examined using a representative FESEM image for Cu₇Te₄ (Fig. 2a). As can be seen, the NPs have a relatively uniform size with different thicknesses. The average thickness of about 42 nm and the average width is about 75 nm. It shows their aggregation and thus inseparability from each other. The average thickness and average width are expected to be larger than the average crystallite size of these NPs. The atomic percentages of constituent elements of Cu, Ag and Te for Cu_{1.94}Ag_{0.06}Te determined from EDX data (Fig. 2b) are 70.50, 3.04 and 26.46. They show excess for Cu and Ag but deficiency for Te compared to their nominal values of 64.7%, 2% and 33.3%. They are attributed to the excess quantity of Cu(CH₃COO)₂·H₂O and Ag₂C₂H₃O₂·H₂O taken during sample preparation as precursors of Cu and Ag. EDX data analysis and Rietveld refinement confirm the atomic percentage of Ag.

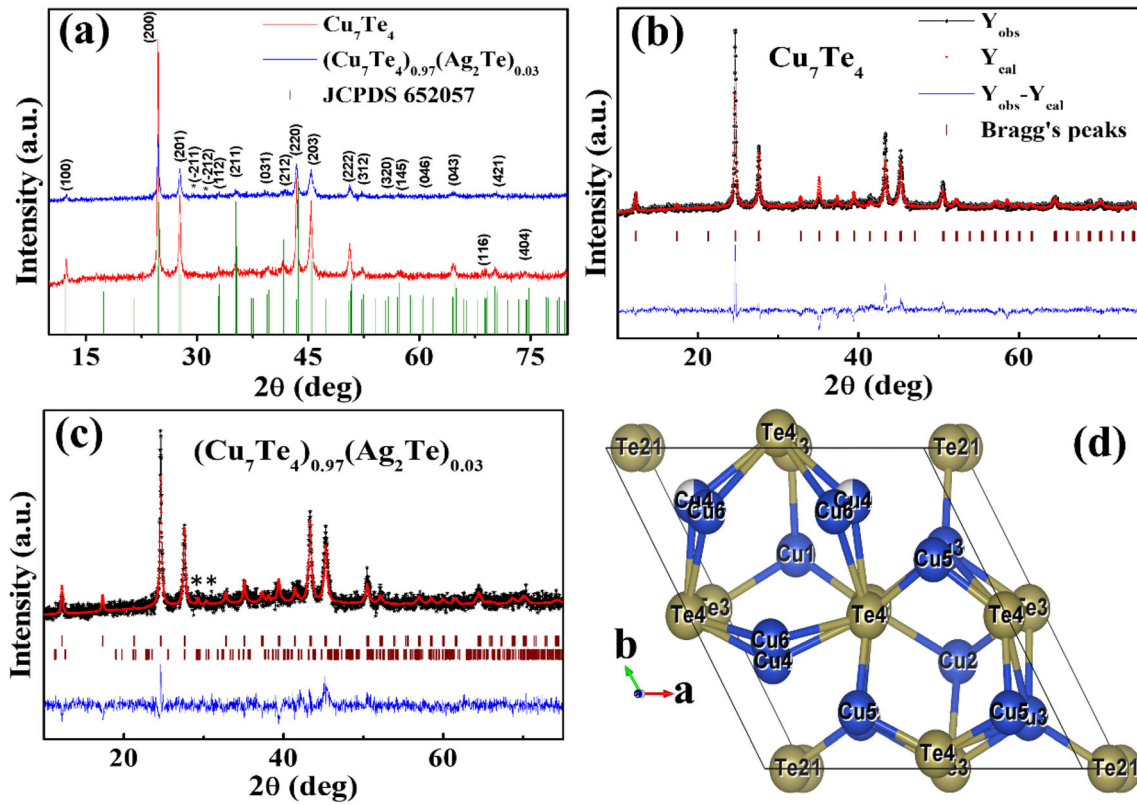


Fig. 1 a XRD patterns with JCPDS, and b–c Rietveld fittings of Cu_7Te_4 and $(\text{Cu}_7\text{Te}_4)_{0.97}(\text{Ag}_2\text{Te})_{0.03}$ showing observed, Rietveld fitting, their difference and Bragg peaks (vertical lines), with star (*) indicating Cu_2Te peaks and d unit cell structure of Cu_7Te_4

Table 1 Lattice parameters, χ^2 , Bragg R factor, RF factor and volume density ρ of the samples

Samples	Phase	a (Å)	b (Å)	c (Å)	V (Å) ³	RF factor	R factor	ρ (g/cm ³)	χ^2	Fraction
Cu_7Te_4	Cu_7Te_4	8.34 (3)	8.34 (3)	7.21(3)	435.57 (0.12)	11.8	23.3	7.43	2.6	100
$(\text{Cu}_7\text{Te}_4)_{0.97}(\text{Ag}_2\text{Te})_{0.03}$	Cu_7Te_4	8.35 (3)	8.35(3)	7.21(3)	435.62 (0.18)	10.4	15.5	7.37	1.5	96.97
	Ag_2Te	8.33 (2)	4.49(3)	9.32(2)	292.66 (1.03)	60.8	93.6	7.79	–	3.03

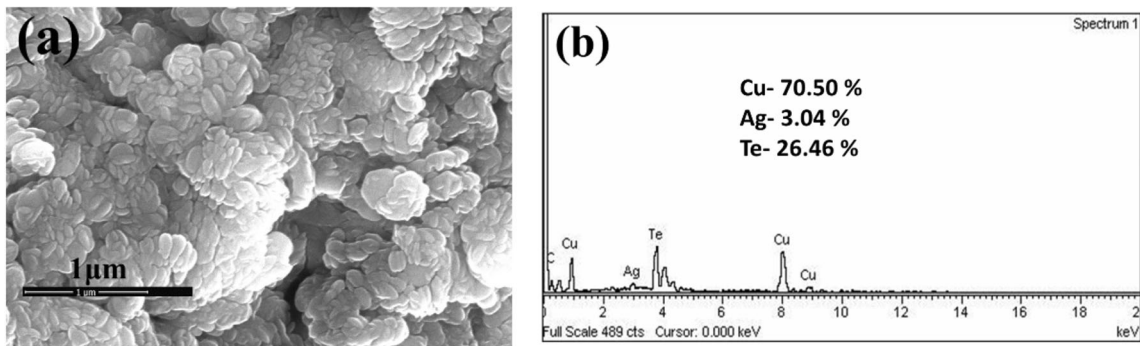


Fig. 2 a FESEM image of Cu_7Te_4 as a representative image and b EDX spectrum of $(\text{Cu}_7\text{Te}_4)_{0.97}(\text{Ag}_2\text{Te})_{0.03}$

3.2 Dynamic light scattering (DLS) study

Intensity distribution of hydrodynamic diameter (HD) and Zeta potential (ζ) at pH = 7 dispersed in deionized water (DIW) for $x = 0, 0.03$ are shown in Fig. 3. It is found that the values of HD are 351 and 308 nm, while those for ζ are -36.8 and -38.2 mV, respectively. HD is much larger than the Scherrer and FESEM size for both the samples, since the aggregation kinetics depend on the mobility of the aggregates or the charge present on the surface of the particles. In general, a greater aggregation of the particles leads to less mobility in a dispersion medium. As a result, the zeta potential is reduced, resulting in a less stable colloidal solution [34]. The values of zeta potential indicate that these NPs are stable in DIW. Li et al. reported that CuTe NPs are highly dispersible in DIW with $\zeta = -55.6$ mV [17]. The ζ value strongly depends on the agglomeration conditions and the interface dipole moment induced between the NP surface and the adsorbate [35]. The order of particle size from the above three techniques is DLS > FESEM > XRD. The information about the crystallite size as obtained by XRD is the region in which atoms are arranged periodically within the inorganic $x = 0, 0.03$ material. FESEM can provide the collective information about the particle size, which would always be the larger and can consist of two or more grains and possibly even grains of different materials. Overall, the DLS makes a collective contribution of the inorganic material and the charged double layer of the agglomerated particle, as determined by the dispersion medium.

3.3 Electrical transport and power factor studies

The metallic temperature-dependent electrical conductivity (σ) for both the samples gradually increases almost exponentially as the temperature is reduced with a slight drop below about 30 K (Fig. 4a). This deviation from linearity is attributed to the possible high degeneracy, change in the DOS and favorable scattering of the charge carriers at the grain boundaries of the nanodisks in the material. The observed values of σ at 325 K are 16.6×10^3 S/m and 15.3×10^3 S/m for $x = 0$ and 0.03, respectively (Table 2). The value of σ changes significantly in $x = 0.03$ NCs compared to that of Cu_7Te_4 as in S values (Fig. 4c). The σ in NC, lower than that of Cu_7Te_4 , is attributed to the lower electrical conductivity (3×10^4 S/m) of Ag_2Te [36] than that (2×10^5 S/m) of Cu_7Te_4 [37]. The observed σ is higher than that in earlier report on Cu_7Te_4 [28]. Zhang et al. [36] observed that the electrical conductivity of a typical semiconductor is determined by trapping the carriers at the grain boundaries or interface between two materials and follows the equation

$$\sigma = Lq^2p \left(\frac{1}{2m^*\pi k_b T} \right)^{0.5} \exp\left(\frac{-E_b}{k_b T} \right), \quad (1)$$

where q is electronic charge, L is grain size, p is average carrier concentration, k_b is Boltzmann constant, m^* is effective mass, T is absolute temperature, and E_b is barrier height at the grain boundaries or at the interfaces. Therefore, the plot of $\ln(\sigma T^{0.5})$ against $1/k_b T$ should be a straight line with E_b as the slope. The values of E_b from the fitting are 1.4 and 4.1 meV for $x = 0$ and 0.03, respectively (Fig. 4b). Increase in barrier height is attributed to the inclusion of Ag_2Te .

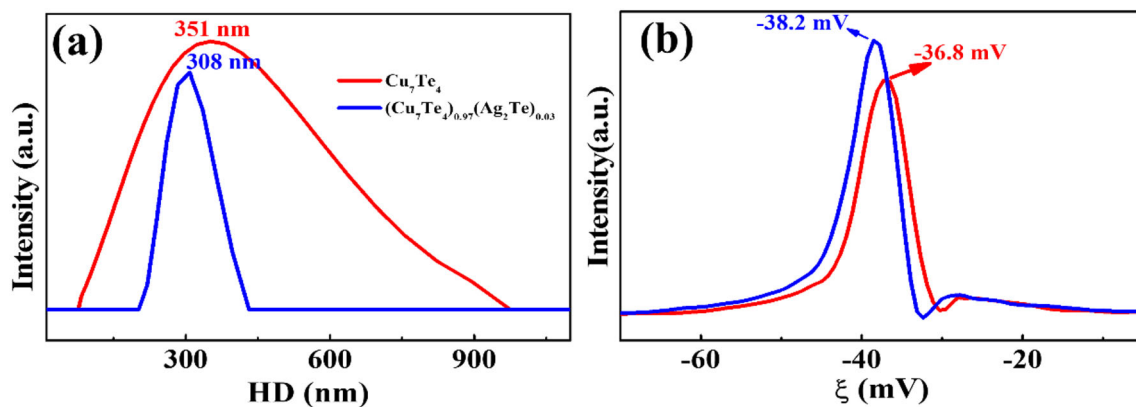


Fig. 3 **a** Hydrodynamic diameter and **b** Zeta potential of Cu_7Te_4 and $(\text{Cu}_7\text{Te}_4)_{0.97}(\text{Ag}_2\text{Te})_{0.03}$ NPs

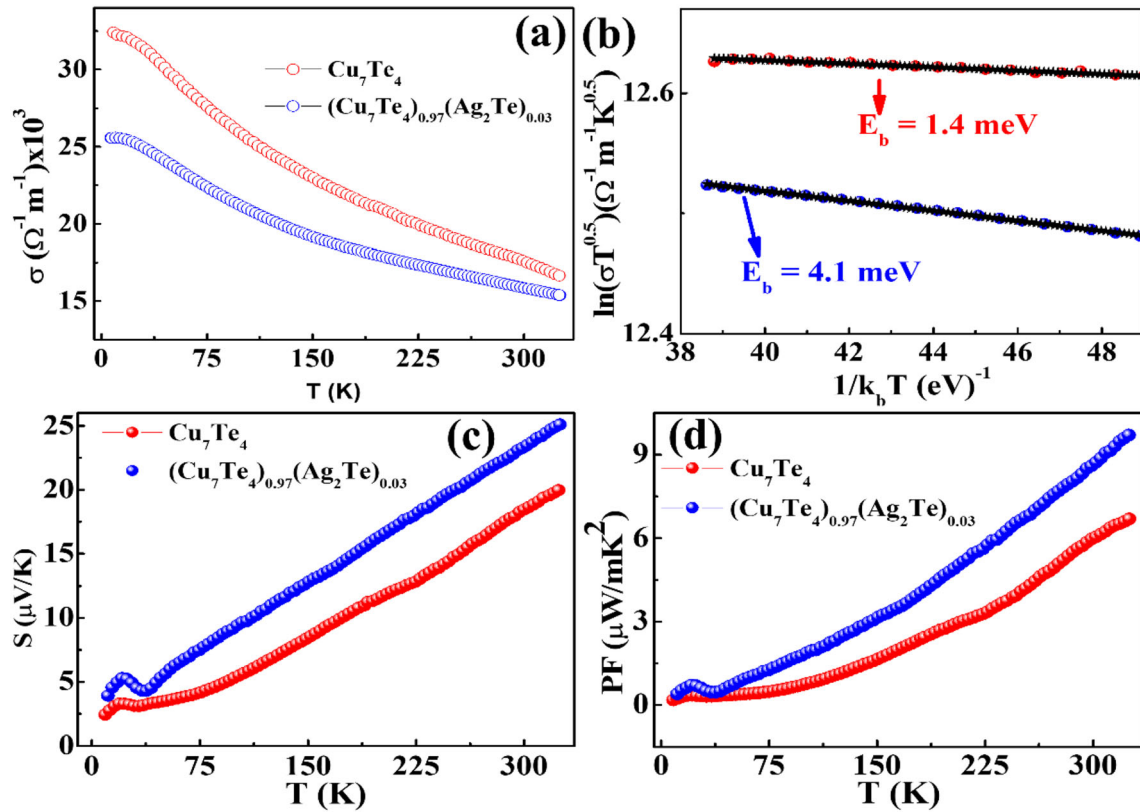


Fig. 4 **a** Electrical conductivity, **b** electrical conductivity fitting of Eq. (1), **c** thermopower and **d** power factor of compacted Cu_7Te_4 and $(\text{Cu}_7\text{Te}_4)_{0.97}(\text{Ag}_2\text{Te})_{0.03}$

Table 2 Comparison of σ , S and PF value at 325 K from some of the references

Sample	σ ($10^3 \Omega^{-1} \text{m}^{-1}$)	S ($\mu\text{V}/\text{K}$)	PF ($\mu\text{W}/\text{mK}^2$)	References
Cu_7Te_4	16.6	20	6.7	Present work
$(\text{Cu}_7\text{Te}_4)_{0.97}(\text{Ag}_2\text{Te})_{0.03}$	15.3	25.1	9.7	
Cu_7Te_4	125	2	5	[20]
Ag_2Te	3	430	0.55	[36]
Bi_2Te_3	125	145	2.6×10^3	[41]

The temperature-dependent S increases with increasing temperature in the entire temperature range (Fig. 4c). It is ~ 20 and $25.1 \mu\text{V}/\text{K}$ at 325 K for $x = 0$ and 0.03 , respectively (Table 2). This means that the S value is 25% higher in $(\text{Cu}_7\text{Te}_4)_{0.97}(\text{Ag}_2\text{Te})_{0.03}$ than that of Cu_7Te_4 . The p-type conduction is confirmed from the positive sign of S , which is consistent with the earlier reports [20, 28]; n-type conduction of Ag_2Te [36, 38] and higher S value than that of p-type Cu_7Te_4 were also reported [28]. However, a small fraction of the Ag_2Te phase simply increases the value of S , but does not affect the sign of S . The majority of the charge carriers in these NPs can also

be holes due to excess of Cu and Ag as seen in EDX data, although not detectable by X-ray diffraction, since they usually have positive thermopower [39]. The small values and the approximately linear behavior of S down to ~ 50 K show the metallic nature of the NPs/NCs in consistent with good electrical conductivity (Fig. 4a). It depends on DOS at the Fermi level (E_F) and a small change in DOS is reflected in the value of S and thus in σ , which can be explained with the Mott expression for metals and degenerate semiconductors:

$$\begin{aligned}
 S &= \frac{\pi^2 k_B}{3 q} k_B T \left\{ \frac{d\{\ln(\sigma(E))\}}{dE} \right\}_{E=E_F} \\
 &= \frac{\pi^2 k_B}{3 q} k_B T \left\{ \frac{1}{n} \frac{dn(E)}{dE} + \frac{1}{\mu} \frac{d\mu(E)}{\mu E} \right\}_{E=E_F} \quad (2) \\
 &\equiv \frac{8\pi^2 k_B^2}{3q\hbar^2} m^* \left(\frac{\pi}{3n} \right)^{\frac{2}{3}},
 \end{aligned}$$

where q , n , m^* and μ are electronic charge, carrier density, effective mass and mobility, respectively. In general, this behavior and the small values of S might also indicate a strongly degenerate hole conduction ($n \sim 10^{20} \text{ cm}^{-3}$) [13]. A small hump close to 20 K is observed due to the interaction between electrons and phonons. We can say from Eqs. (1) and (2) that as the value of E_b increases, the value of S also increases with decreasing σ due to the electron filtering effect [12, 13, 36, 40]. Hence, $(\text{Cu}_7\text{Te}_4)_{0.97}(\text{Ag}_2\text{Te})_{0.03}$ has higher S and lower σ than those of Cu_7Te_4 . Inorganic and organic thermoelectric materials have suggested that the optimized barrier height be in the range of 0.05–0.1 eV [36, 40]. In our case, however, it is very low, which indicates that Cu_7Te_4 and $(\text{Cu}_7\text{Te}_4)_{0.97}(\text{Ag}_2\text{Te})_{0.03}$ NPs/NCs are highly degenerate semiconductors.

The PF as an electrical part of a thermoelectric material increases with increasing temperature (Fig. 4d). It is ~ 6.7 and $9.7 \mu\text{Wm}^{-1} \text{K}^{-2}$ at 325 K for $x = 0$ and 0.03, respectively (Table 2). This p–n-type combination of $(\text{Cu}_7\text{Te}_4)_{0.97}(\text{Ag}_2\text{Te})_{0.03}$ NCs shows an increase in its PF by $\sim 45\%$ compared to that of Cu_7Te_4 , 94% more than of $\text{Cu}_{1.75}\text{Te}$ nanosheet [20] and 242 times higher than that of $\text{Bi}_{2-x}\text{Cu}_x\text{S}_3$ [42]. They clearly show the very interesting nature of this work.

4 Conclusions

In summary, we have successfully synthesized $(\text{Cu}_7\text{Te}_4)_{1-x}(\text{Ag}_2\text{Te})_x$ ($x = 0, 0.03$) NCs using the polyol method. XRD shows that their average particle size is approximately in 23–31 nm range. FESEM shows that the average thickness of Cu_7Te_4 NPs is about 42 nm and the average width is about 75 nm. HD is found to be in the range of 308–351 nm and zeta potential values indicate that these NCs are stably dispersed in DIW. The electrical conductivity of these NPs decreases almost exponentially with decrease in temperature and shows their degenerate

semiconducting behavior with high electrical conductivity. The positive sign of thermopower of these NCs indicates a p-type conduction. The power factor at 325 K for $(\text{Cu}_7\text{Te}_4)_{0.97}(\text{Ag}_2\text{Te})_{0.03}$ is 242 times larger than that found in $\text{Bi}_{2-x}\text{Cu}_x\text{S}_3$ [42] and 45% increase compared to that of Cu_7Te_4 . These results are rather encouraging and would open a new window to improve TE performances at 325 K.

Acknowledgements

The authors thank M. Gupta/Layanta Bahera for XRD data, R. Venkatesh for FESEM and DM Phase/VK Ahire for EDAX data, UGC-DAE consortium for scientific research, Indore, MP, India.

Author contributions

CC prepared all the samples, did measurements and manuscript drafting, GSO corrected this manuscript and BM helps in measurements and sample synthesis. All authors approve to this submission.

Funding

This work was supported by UGC-DAE Consortium for Scientific Research, University Campus, Khandwa Road, Indore-452001, Madhya Pradesh, India.

Compliance with ethical standards

Conflicts of interest The authors declare that they have no conflict of interest.

Electronic supplementary material: The online version of this article (<https://doi.org/10.1007/s10854-020-04610-1>) contains supplementary material, which is available to authorized users.

References

1. F. Bonaccorso, L. Colombo, G. Yu, M. Stoller, V. Tozzini, A.C. Ferrari, R.S. Ruoff, V. Pellegrini, *Science* **347**, 6217 (2015)
2. L.D. Zhao, S.H. Lo, Y. Zhang, H. Sun, G. Tan, C. Uher, C. Wolverton, V.P. Dravid, M.G. Kanatzidis, *Nature* **508**, 373 (2014)

3. A.T. Duong, V.Q. Nguyen, G. Duvjir, V.T. Duong, S. Kwon, J.Y. Song, J.K. Lee, J.E. Lee, S. Park, T. Min, J. Lee, J. Kim, S. Cho, *Nat. Commun.* **7**, 131713 (2016)
4. Tarachand, B. Mukherjee, M. Saxena, Y. K. Kuo, G. S. Okram, S. Dam, S. Hussain, A. Lakhani, U. Deshpande, and T. Shripathi, *ACS Appl. Energy Mater.* **2**, 6383 (2019).
5. M.G. Kanatzidis, *Chem. Mater.* **22**, 648 (2010)
6. Z.H. Ge, B.P. Zhang, Y.X. Chen, Z.X. Yu, Y. Liu, J.F. Li, *Chem. Commun.* **47**, 12697 (2011)
7. J.P. Heremans, V. Jovicic, E.S. Toberer, A. Saramat, K. Kurosaki, A. Charoenphakdee, S. Yamanaka, G.J. Snyder, *Science* **321**, 1457 (2008)
8. Y. Pei, X. Shi, A. Lalonde, H. Wang, L. Chen, G.J. Snyder, *Nature* **473**, 66 (2011)
9. J.H. Bahk, Z. Bian, A. Shakouri, *Phys. Rev. B Condens. Matter Mater. Phys.* **87**, 075204 (2013)
10. J.M.O. Zide, D. Vashaee, Z.X. Bian, G. Zeng, J.E. Bowers, A. Shakouri, A.C. Gossard, *Phys. Rev. B Condens. Matter Mater. Phys.* **74**, 1 (2006)
11. D. Vashaee, A. Shakouri, *Phys. Rev. Lett.* **92**, 10 (2004)
12. S.V. Faleev, F. Léonard, *Phys. Rev. B Condens. Matter Mater. Phys.* **77**, 214304 (2008)
13. M. He, J. Ge, Z. Lin, X. Feng, X. Wang, H. Lu, Y. Yang, F. Qiu, *Energy Environ. Sci.* **5**, 8351 (2012)
14. T. Ishibe, A. Tomeda, K. Watanabe, Y. Kamakura, N. Mori, N. Naruse, Y. Mera, Y. Yamashita, Y. Nakamura, A.C.S. *Appl. Mater. Interfaces* **10**, 37709 (2018)
15. Y. He, T. Zhang, X. Shi, S.H. Wei, L. Chen, *NPG Asia Mater.* **7**, e210 (2015)
16. S. Ballikaya, H. Chi, J.R. Salvador, C. Uher, *J. Mater. Chem. A* **1**, 12478 (2013)
17. W. Li, R. Zamani, P. Rivera Gil, B. Pelaz, M. Ibáñez, D. Cadavid, A. Shavel, R.A. Alvarez-Puebla, W.J. Parak, J. Arbiol, A. Cabot, *J. Am. Chem. Soc.* **135**, 7098 (2013)
18. A.C. Poulouse, S. Veeranarayanan, M.S. Mohamed, Y. Sakamoto, T. Maekawa, D.S. Kumar, *Sci. Rep. Nat. Publ. Gr.* **6**, 35961 (2016)
19. L.P. Tan, T. Sun, S. Fan, L.Y. Ng, A. Suwardi, Q. Yan, H.H. Hng, *Nano Energy* **2**, 4 (2013)
20. C. Nethravathi, C.R. Rajamathi, M. Rajamathi, R. Maki, T. Mori, D. Golberg, Y. Bando, *J. Mater. Chem. A* **2**, 985 (2014)
21. T. Willhammar, K. Sentosun, S. Mourdikoudis, B. Goris, M. Kurtepeli, M. Bercx, D. Lamoen, B. Partoens, I. Pastoriza-Santos, J. Pérez-Juste, L.M. Liz-Marzán, S. Bals, G. Van Tendeloo, *Nat. Commun.* **8**, 1 (2017)
22. Y. Ni, H. Zhang, J. Xi, X. Wang, Y. Zhang, Y. Xiao, X. Ma, J. Hong, *CrystEngComm* **16**, 7869 (2014)
23. P. Kumar, K. Singh, *Cryst. Growth Des.* **9**, 3089 (2009)
24. B. Li, Y. Xie, J. Huang, Y. Liu, Y. Qian, *Chem. Mater.* **12**, 2614 (2000)
25. Y. Zhang, Y. Ni, X. Wang, J. Xia, J. Hong, *Cryst. Growth Des.* **11**, 4368 (2011)
26. Q. Wang, G. Chen, X. Shi, R. Jin, L. Wang, D. Chen, *Powder Technol.* **207**, 192 (2011)
27. Tarachand, S. Hussain, N. P. Lalla, Y. K. Kuo, A. Lakhani, V. G. Sathe, U. Deshpande, and G. S. Okram, *Phys. Chem. Chem. Phys.* **20**, 5926 (2018).
28. C. Chotia, Tarachand, V. Sharma, R. Venkatesh, and G. S. Okram, in *AIP Conf. Proc.* **2115**, 030066 (2019).
29. Tarachand, M. Saxena, B. Mukherjee, and G. S. Okram, *Rev. Sci. Instrum.* **90**, 063904 (2019).
30. A. Soni, G.S. Okram, *Rev. Sci. Instrum.* **79**, 125103 (2008)
31. W. Shi, L. Zhou, S. Song, J. Yang, H. Zhang, *Adv. Mater.* **20**, 1892 (2008)
32. K. Momma, F. Izumi, *J. Appl. Crystallogr.* **44**, 1272 (2011)
33. I.R. Amiraslanov, N.A. Alieva, G.G. Guseinov, G.M. Agamirzoeva, *Crystallogr. Rep.* **62**, 210 (2017)
34. V. Sharma, C. Chotia, Tarachand, V. Ganesan, G.S. Okram, *Phys. Chem. Chem. Phys.* **19**, 14096 (2017)
35. V. Sharma, D. Verma, G.S. Okram, R.J. Choudhary, *J. Magn. Magn. Mater.* **497**, 166000 (2020)
36. M. Zhang, H. Park, J. Kim, H. Park, T. Wu, S. Kim, S.D. Park, Y. Choa, N.V. Myung, *Chem. Mater.* **27**, 5189 (2015)
37. A. Ghosh, M. Mitra, D. Banerjee, A. Mondal, *RSC Adv.* **6**, 22803 (2016)
38. S. Lee, H.S. Shin, J.Y. Song, M. Jung, *J. Nanomaterials* **2017**, 14 (2017). <https://doi.org/10.1155/2017/4308968>
39. G.S. Okram, N. Kaurav, *J. Appl. Phys.* **110**, 023713 (2011)
40. A. Popescu, L.M. Woods, J. Martin, G.S. Nolas, *Phys. Rev. B Condens. Matter Mater. Phys.* **79**, 1 (2009)
41. W. Wu, W. Liu, F. Yu, *J. Mater. Sci. Mater. Electron.* **31**, 1200 (2020)
42. Tarachand, V. Sharma, R. Bhatt, V. Ganesan, and G. S. Okram, *Nano Res.* **9**, 3291 (2016).

Publisher's Note Springer Nature remains neutral with regard to jurisdictional claims in published maps and institutional affiliations.